Supporting Information (SI) for "Characterizing Ensembles of Plate-like Particles via Machine Learning"

Anna Jaeggi[1], Ashwin Kumar Rajagopalan[1,¶], Manfred Morari[2], and Marco Mazzotti[1,*]

[1]Institute of Energy and Process Engineering, ETH Zurich, 8092 Zurich, Switzerland

[2]Department of Electrical and Systems Engineering, University of Pennsylvania, Philadelphia, Pennsylvania 19104, United States

[¶]Current Address: Department of Chemical Engineering, Imperial College London, SW7 2AZ, United Kingdom

[*]Email: marco.mazzotti@ipe.mavt.ethz.ch

In this supporting information (SI), additional material that was not covered in detail in the main text of the article is provided. In Section S1, a schematic of the dual projection imaging setup and an illustration of the different bounding box algorithms used in this work is provided. In Sections S2.1 and S2.2, the errors of *method 1* (dual projection imaging coupled with an oriented bounding box) arising due to alignment and aspect ratio dependence of additional estimated quan-

tities, i.e. the lengths L_1 and L_2, and the volume V are discussed. In Section S3, the impact of platelet alignment in a triple projection setup is discussed. In Section S4, the details of model training and model performance for the machine learning modeling techniques are discussed. Finally, in Section S5, the population balance equation framework, the operating conditions, and the kinetic parameters used in the population balance equation solver to simulate a growth-dominated batch cooling crystallization process are provided.

S1 Imaging Device

S1.1 Schematic of the Dual Imaging Setup (DISCO)

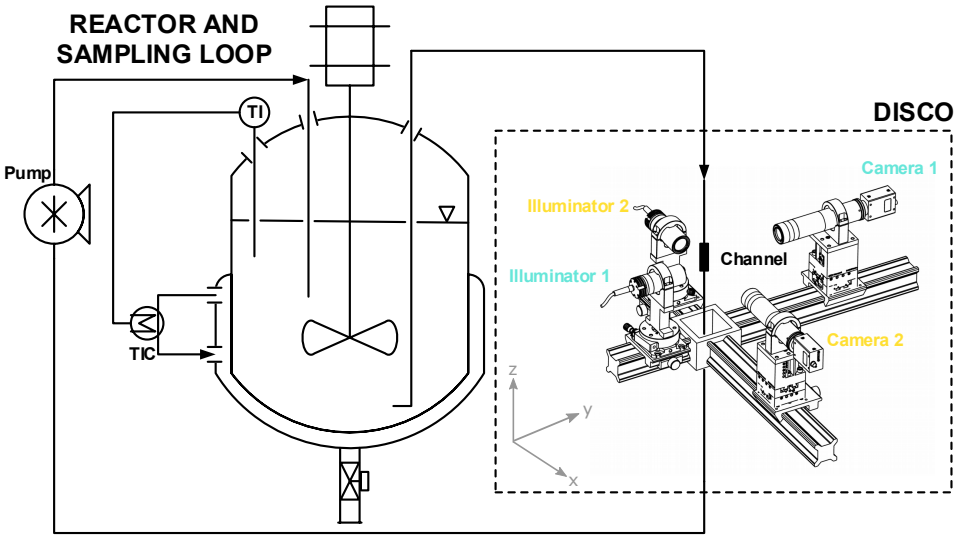

Figure S1: Schematic of the experimental setup (in a laboratory setting) coupled with the dual imaging system for crystallization observation (DISCO). The suspension flows from the reactor through the flow channel that is back illuminated using two telecentric illuminators. The suspension is imaged using two cameras with telecentric optics. The actual experimental setup was not used in this work, but it dictates the positioning of the imaging planes in this work.

S1.2 Bounding Box Algorithms

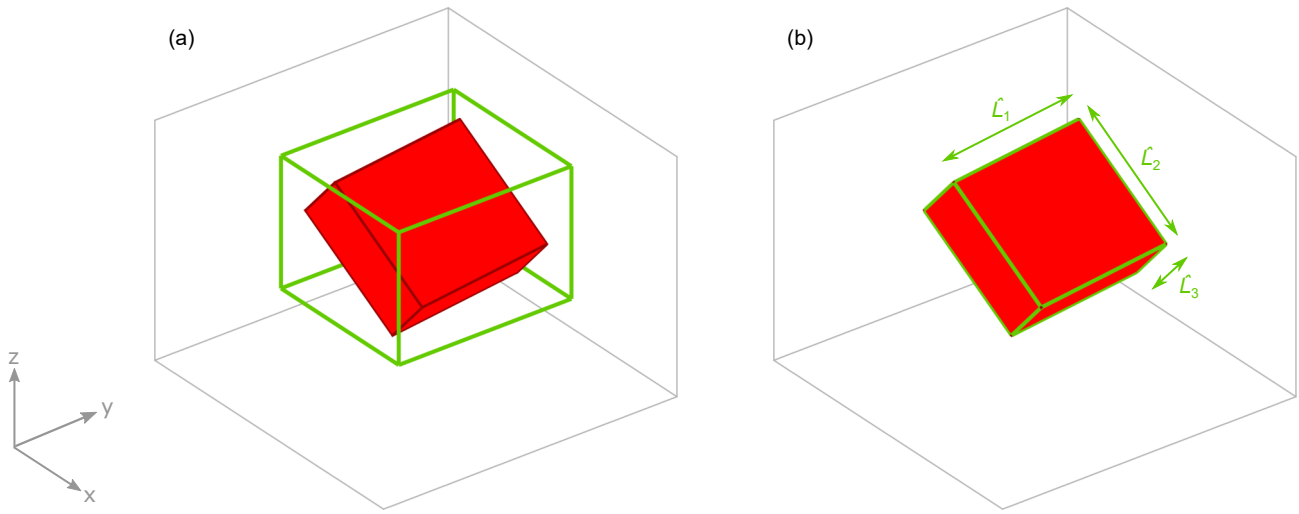

Figure S2: Illustration of the two bounding box algorithms used in this work. Panel (a) shows the axis-aligned bounding box (green edges), used previously,[1] and panel (b) shows the object oriented bounding box used extensively in this article. The particle (red) in both panels (a) and (b) share the same lengths and same orientation.

S2 Further Comments on the Performance of Method 1

S2.1 Sensitivity to Particle Alignment

The influence of the particle alignment on the accuracy of the estimated thickness $\hat{L}_3$ using *method 1* is discussed in Section 3 of the main text. However, the particle alignment also has an impact on the characterization accuracy of the other two lengths $\hat{L}_1$ and $\hat{L}_2$, but to a lesser extent, and on the estimated volume $\hat{V}$, similar to $\hat{L}_3$. These effects are presented here for the same population and angle distributions as in Section 3.1 of the main text. The errors on L_1 and L_2 are significantly smaller when compared to the errors on L_3 and V. However, the random alignment case (red, case (3) in Section 3.1 of the main text) is clearly the most problematic case for all the estimated

quantities. The errors in the estimated lengths $\hat{L}_1$ and $\hat{L}_2$ can be attributed to certain alignment cases in which the largest plane of the particle is aligned towards one of the two cameras at an angle that leads to a reduction in the estimated particle lengths along L_1 and/or L_2. Additionally, this reduction due to the unfavorable alignment can also cause L_1 and L_2 to be swapped during the characterization process, leading to an additional source of error. The distributions of errors on V resembles the distribution of errors on L_3 and a plausible explanation for this is visualized in Figure 2 of the main text.

S2.2 Sensitivity to Aspect Ratio

The influence of aspect ratio on the characterization error on the particle lengths and the particle volume for *method 1* is discussed in Section 3.2 of the main text and Figure 2 of the main text. The aspect ratio effects along the two larger lengths L_1 and L_2 leads to comparatively small errors and a brief discussion on these errors is presented here. Figure 4 of the main text reveals a slight aspect ratio dependence of the estimated largest length $\hat{L}_1$. The error is high at low aspect ratios, i.e. for particles that are equant. The cause of this effect can be explained using the example case visualized in Figure S4a. For L_1, the biggest possible overestimation occurs when two space diagonals of the particle are parallel to the imaging planes. In that case, $\hat{L}_1$ will be equal to the space diagonal $\sqrt{L_1^2 + L_2^2 + L_3^2}$ instead of L_1. The space diagonal is largest at an aspect ratio of one (both L_1/L_2 and L_2/L_3), because at these aspect ratios all lengths are equally large, leading to a larger overestimation. As L_2 and L_3 become smaller relative to L_1, the space diagonal approaches L_1, leading to smaller errors. Note that on a population scale however, the worst overestimation of L_1 is around 40 % among all the cases considered here.

As for the aspect ratio dependence of L_2, Figure 4 of the main text shows that the second largest

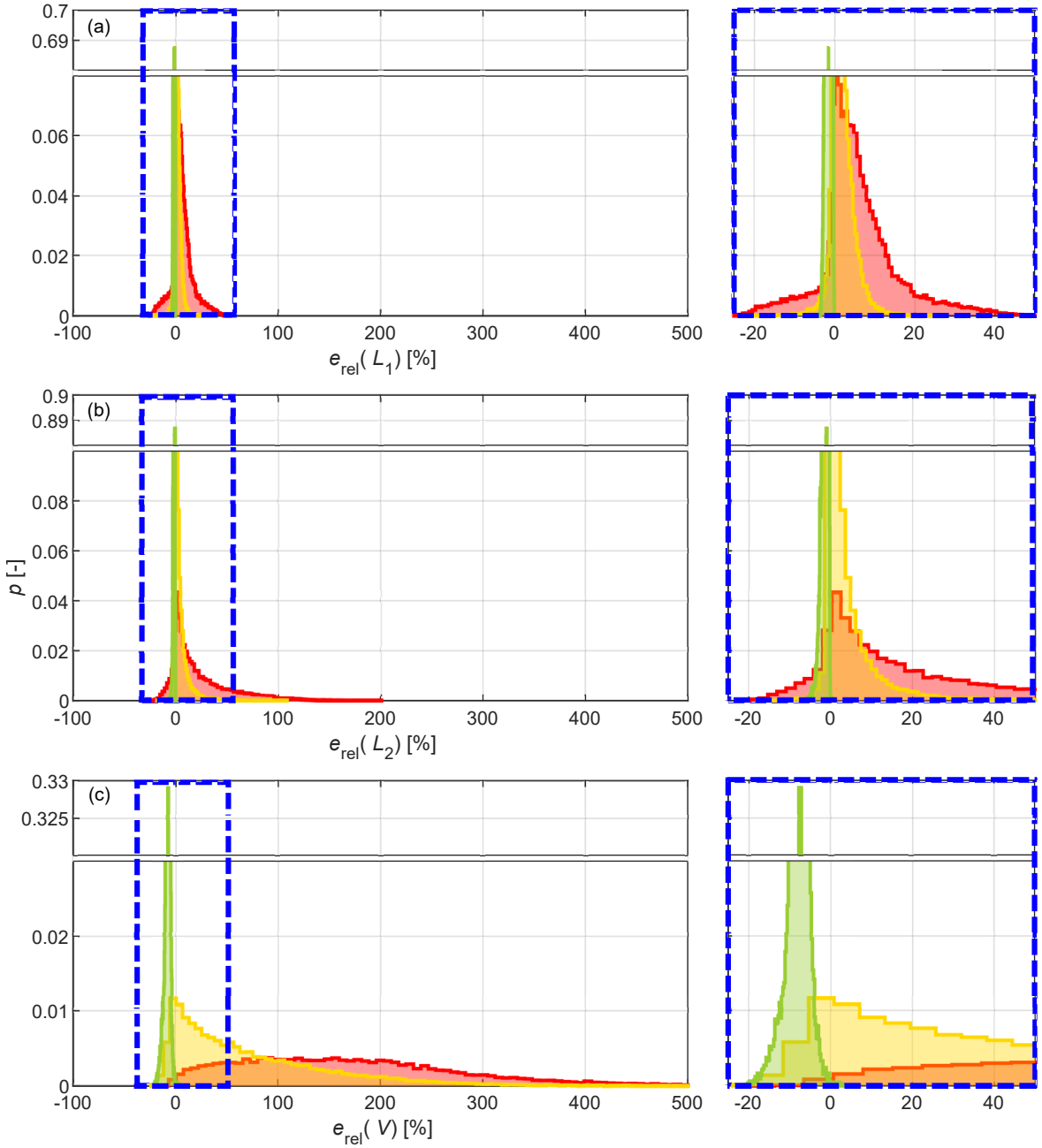

Figure S3: Distribution of the relative error on the (a) largest length $e_{\text{rel}}(L_1)$, (b) second largest length $e_{\text{rel}}(L_2)$, and (c) the reconstructed visual hull volume $e_{\text{rel}}(V)$, obtained using Equation 1 of the main text, for a population of particles with the three different angle distributions from panel (a) of Figure 3 of the main text. Note that these distributions share the same color code with Figure 3 of the main text and *method 1* is used. Zoomed in version of the plots for the region of interest (blue dotted box) are provided on the right hand side.

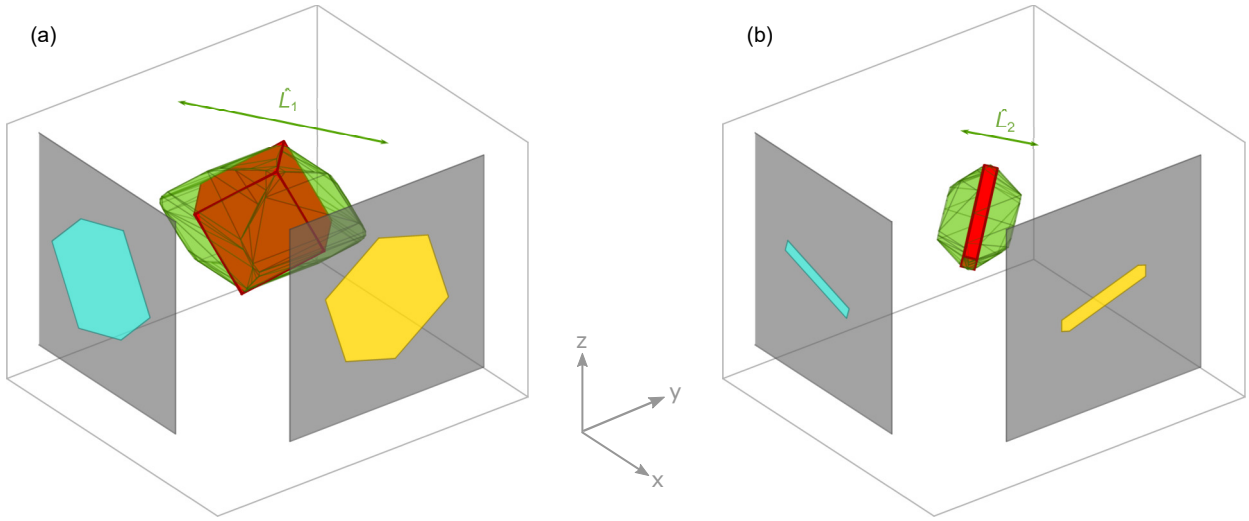

Figure S4: Schematic representation of a perfect (a) equant particle (red) and (b) needle-like particle (red), their projections (cyan/yellow shaded polygon) onto the two imaging planes (grey) representing the perspective observed by two independent cameras, and the reconstructed volume obtained using two projections (green volume). Qualitative representation of the relevant particle lengths L_i that can be estimated from the 3D reconstruction (green volume) is also illustrated.

length L_2 for needle-like particles is prone to large errors when using the bounding box approach to compute the lengths. The reason for this is illustrated in Figure S4b. When these needles aren't parallel to either of the two imaging planes and are aligned at a 45° angle to both imaging planes, the reconstructed visual hull can resemble a platelet (as discussed previously[1]). The needle that is reconstructed as a platelet has a higher L_2 when compared to the needle it's derived from. In the most extreme case, L_2 will be estimated as $\hat{L}_2 = \frac{\sqrt{2}}{2} L_1$, where L_1 is the true needle length. Even though these cases are rare, they can contribute significantly to the average relative error on a population scale.

It is important to note that this effect only occurs when using the 3D oriented bounding box approach. In the existing image analysis pipeline, lengths of the particles classified as needles are obtained by imposing a generic shape of a cylinder with only length L_1 and width L_2 as the char-

acteristic lengths. Note that in this case L_2 is equivalent to the L_3 in the 3D analysis with the bounding box approach. Also in the experimental setup (see Section S1) needles are unlikely to be oriented perpendicular to the flow direction. Therefore, a population of needle-like crystals does not suffer from the effect described here.

S3 Further Comments on the Performance of Method 2

This section provides visual examples for the favorable and unfavorable alignment cases when using *method 2* (an additional third projection in the existing dual projection imaging setup), as described in Section 4.1 of the main text. In Figure S5, three identical platelets (red) aligned at three different orientations with respect to the three imaging planes are visualized. The two projections used in *method 1* are indicated in cyan and yellow, and the additional projection is highlighted in magenta. The reconstructed visual hull obtained using the two projections is superimposed in green and the reconstructed visual hull obtained using all three projections is superimposed in magenta.

Figure S5a shows a case where the third camera significantly improves the estimation of the platelet thickness and volume. In this case, the thin side of the particle is facing the third camera, therefore, the reconstructed visual hull obtained by using only two cameras (green) is significantly larger than the one using all three cameras (see Section 3.1 of the main text). Figure S5b shows an alignment in which the reconstructed visual hull using three projections is a hexagonal prism. The visual hull volume is significantly reduced by introducing an additional projection, however, the thickness of the particle remains practically identical to the thickness estimated with two projections. The reason for this is that the particle lengths are obtained using an oriented bounding box, which fits a cuboid over a reconstructed particle. When this bounding box is fitted to a hexagonal prism,

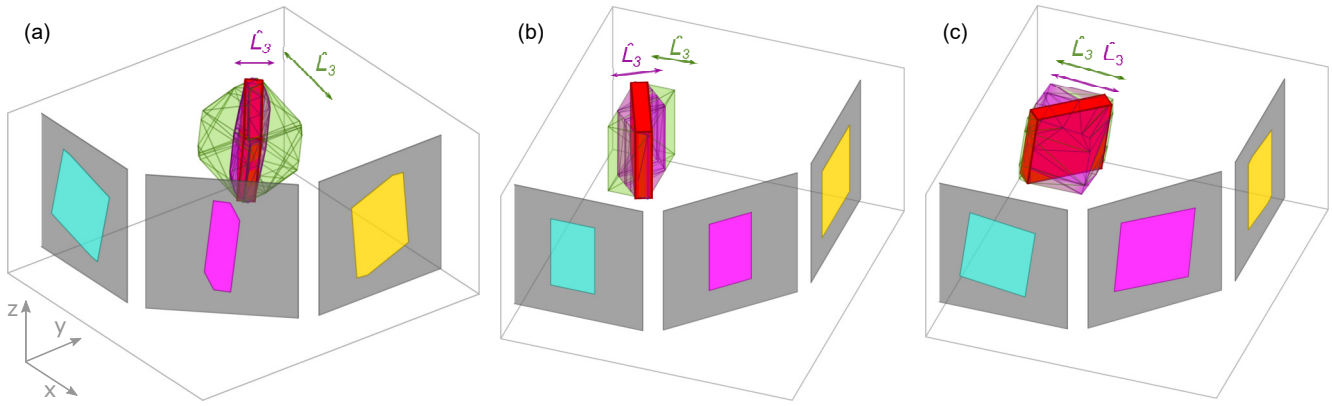

Figure S5: Schematic representation of a platelet (red volume), it's projection (cyan/yellow/magenta shaded polygon) onto the three imaging planes (gray) representing the perspective observed by three independent cameras, and the reconstructed volume obtained using two projections (green volume) and three projections (magenta volume). The particle thickness L_3 that can be estimated from the 3D reconstruction (green/magenta volumes) is also illustrated. Also, the particles shown in panels (a), (b), and (c) are identical in terms of their true lengths and they differ only in their orientation with respect to the imaging planes.

the bounding box thickness is identical to the bounding box thickness of the visual hull obtained from two projections for a particle that fills the entire visual hull volume. Figure S5c displays the worst possible alignment for the triple projection setup. The platelet thickness is not visible from any of the three cameras. The projections cast on all the cameras are equant rectangles, and hence the reconstructed visual hull is also an equant body. This leads to a situation where the volumetric reconstructions using both dual and triple projections are identical, i.e. neither the volume nor the thickness is improved by the introduction of an additional projection.

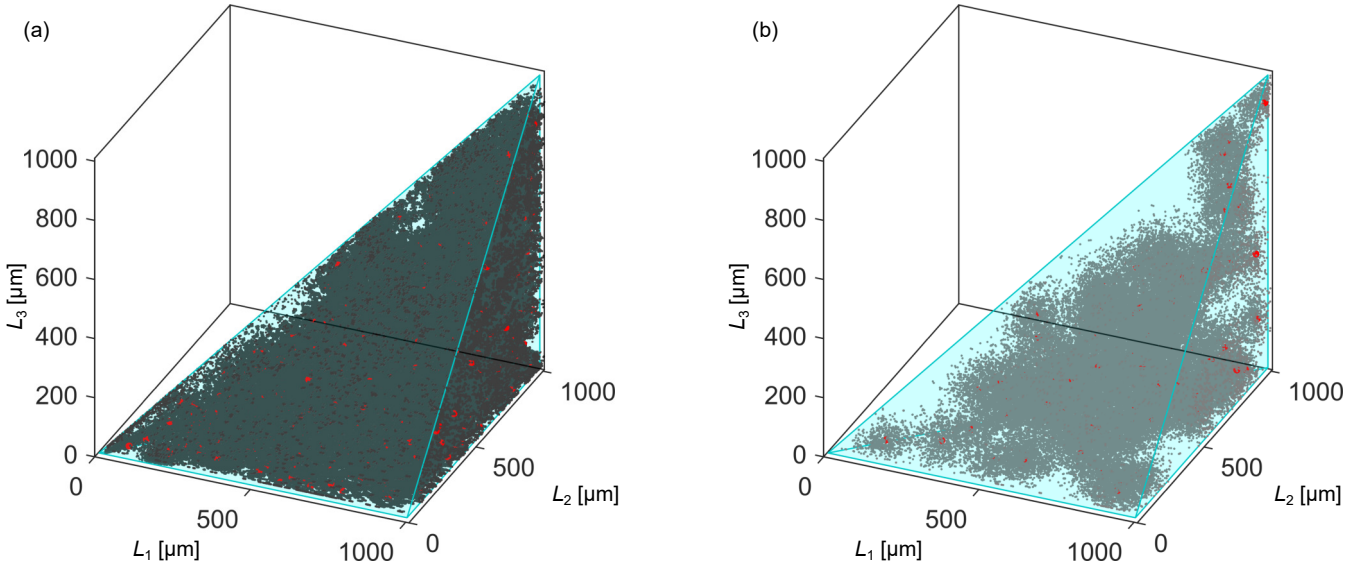

Figure S6: Particle lengths of all the sampled particles used for (a) model training and for (b) model validation. For model training, a total of 990 000 particles was used and for the model validation, a total of 100 000 particles was used. The red markers in the two panels indicate the average lengths of the particle populations from which the sampled particles (gray) are derived from. Note that the lengths of the sampled particle are bound by the cyan region due to the constraints: $L_1 \geq L_2$, $L_2 \geq L_3$, the maximum observable sizes by the camera and the minimum resolution of the camera.

S4 Further Comments on the Performance of Method 3

S4.1 Data Sampling

Figure S6 illustrates the lengths of the particles used for the machine learning model in the training set and the validation set.

S4.2 Feature Elimination

As mentioned in Section 4.2 of the main text, feature elimination was undertaken to reduce the complexity of the data driven model. A more detailed discussion of the same feature elimination is provided here. Figure S7 shows a heat map that illustrates the correlation of the 22 features used in

this study with each other. The features eliminated by the correlation elimination step are the visual hull omnivariance (feature 9), the visual hull anisotropy (feature 10), and the sum of all eigenvalues of the visual hull (feature 12) (indicated in red).

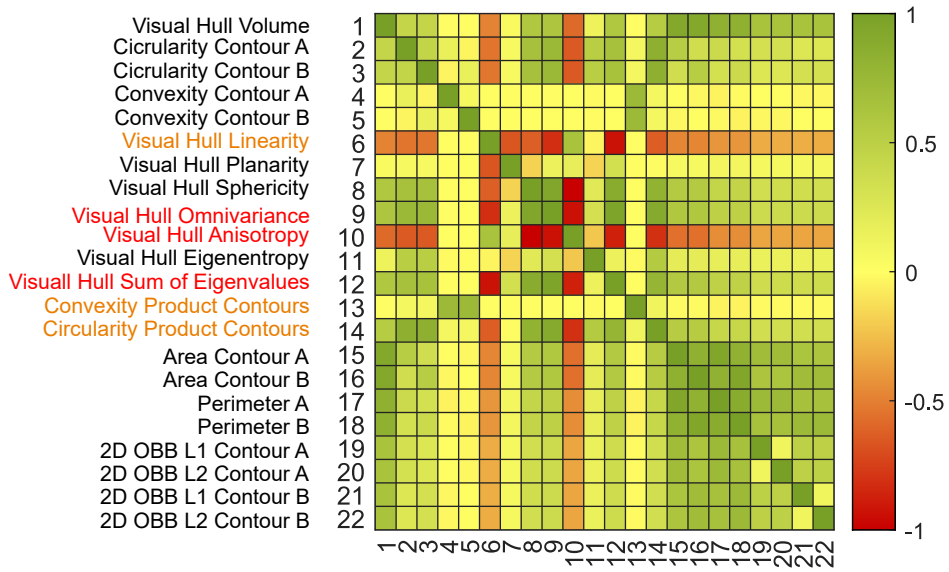

Figure S7: Heatmap illustrating the correlation of the 22 features used in this study with each other. The features highlighted in red are the ones that were eliminated by the correlation elimination step due to high correlation. The features in orange are the ones that were eliminated due to the recursive feature elimination. Note that 1 indicates positive correlation and -1 indicates negative correlation.

The recursive feature elimination first eliminated the product of the circularity of the two contours (feature 14), then the product of the convexity of the two contours (feature 13), and finally the visual hull linearity (feature 6). The information of the circularity and convexity of the contours is already contained in features two through five. The products of these shape features might have been eliminated as the individual shape features are more informative to the model. For the elimination of the visual hull linearity there is no obvious explanation, but the fact that it could be removed without decreasing the model performance in cross validation shows that it does not seem to contain useful information that can be exploited to estimate the lengths by this specific model.

The recursive feature elimination was terminated after eliminating these three features.

S4.3 Model Performance of Supervised Learning Techniques

As mentioned in Section 4.2 of the main text, various modeling techniques were tested before finalizing on artificial neural networks as the model of choice. For neural networks the hyperparameters that are optimized are the number of layers, ranging from one to three, and the number of nodes, ranging from 30 to 100 in steps of 10. The optimal parameters in the neural network optimization were three layers and 100 neurons, which is at the boundary of the tested domain. Therefore it could be that a better performance could be achieved with more layers and/or more nodes per layers. However, due to the larger computational effort involved, a broader region was not explored. As described in the main text, the simplest model within one standard deviation of the best performing model was chosen, which in this case is two layers with 50 neurons. For the regression tree model the number of splits was optimized. Values between three and 10 were tested and compared. For the SVM model, different kernels, namely linear, RBF/ Gaussian, and polynomial, with different halves of the widths of the epsilon intensive band ranging from 0.01 to 100, and different polynomial degrees ranging from one to three (in the case of a polynomial kernel) were compared. The hyperparameters for each of these three techniques and their optimal performance (in terms of the relative error along the three lengths) are listed in Table S1. Note that for all methods besides ANN, the multiple outputs (characteristic lengths) were obtained by training a model for each of them with the same hyperparameters.

Table S1: Optimal performance on the test set for the different supervised techniques $e_{\mathrm{rel}}(L_{\mathrm{i}})$ [%].

	$e_{\mathrm{rel}}(L_1)$	$e_{\mathrm{rel}}(L_2)$	$e_{\mathrm{rel}}(L_3)$
Feedforward Neural Net (layers = 2, nodes per layers = 50)	4	11	33
Regression Tree (no. splits = 7)	44	60	86
Support Vector Machines (kernel = polynomial, degree = 3, epsilon = 20)	33	74	180

S4.4 Performance Evaluation of Artificial Neural Network Based Predictive Model

In the main text of the article, a comparison of the different characterization methods and their associated errors on a test set (Section 4 of the main text) are reported. Additionally, the particle alignment (see Section 3.1 of the main text) and aspect ratio (see Section 3.2 of the main text) dependence of the characterization error for *method 1* is also reported. For the machine learning model, the particle alignment (or the distribution of angles) should not greatly influence the characterization error, as the model is trained on individual particles which were created with a uniform distribution of alignment angles with respect to the cameras. Therefore, the presence of different particle alignment cases in the training data set affects the model performance on all these three angle distribution cases. Since the real angle distribution in the experimental setup (see Section S1 of the main text) is unknown, it is important to ensure that none of the realistic angle distributions result in extreme errors, which is confirmed in Figure S8. This figure illustrates the average relative error along the three lengths L_{i} (columns) for the three alignment cases (rows) and the different average aspect ratios (x/y axis) for*method 3*using a reference population ($\bar{L}_1/\bar{L}_2 = 1$ and $\bar{L}_2/\bar{L}_3 = 1$) of average length $\bar{L}_{1,\mathrm{n}} = 150\,\mu\mathrm{m}$.

To analyze the influence of particle size on the characterization accuracy, both the *method 1*

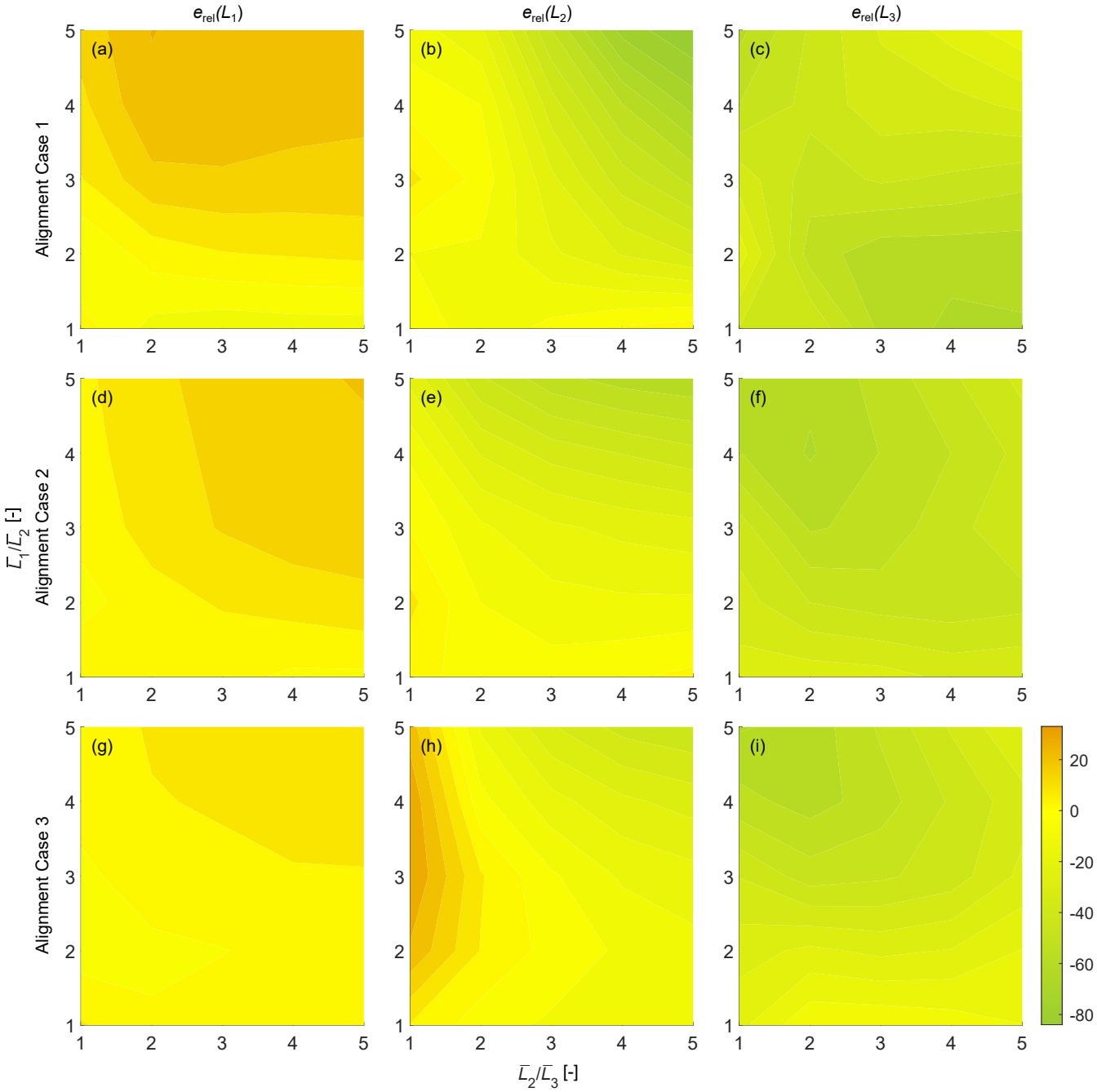

Figure S8: 2D contour plots of the average relative error e_{rel} of the average lengths (a,d,g) L_1, (b,e,h) L_2 and (c,f,i) L_3 obtained using *method 3* as a function of the average aspect ratios of the true population $\bar{L}_1/\bar{L}_2$ and $\bar{L}_2/\bar{L}_3$. Note that the relative error is computed using the number-weighted average over the entire true population and estimated population.

and *method 3* were tested (similar to the study reported in Section 3.2 of the main text). The same combinations of aspect ratios were tested for different populations with reference length $\bar{L}_{1,\text{n}}$

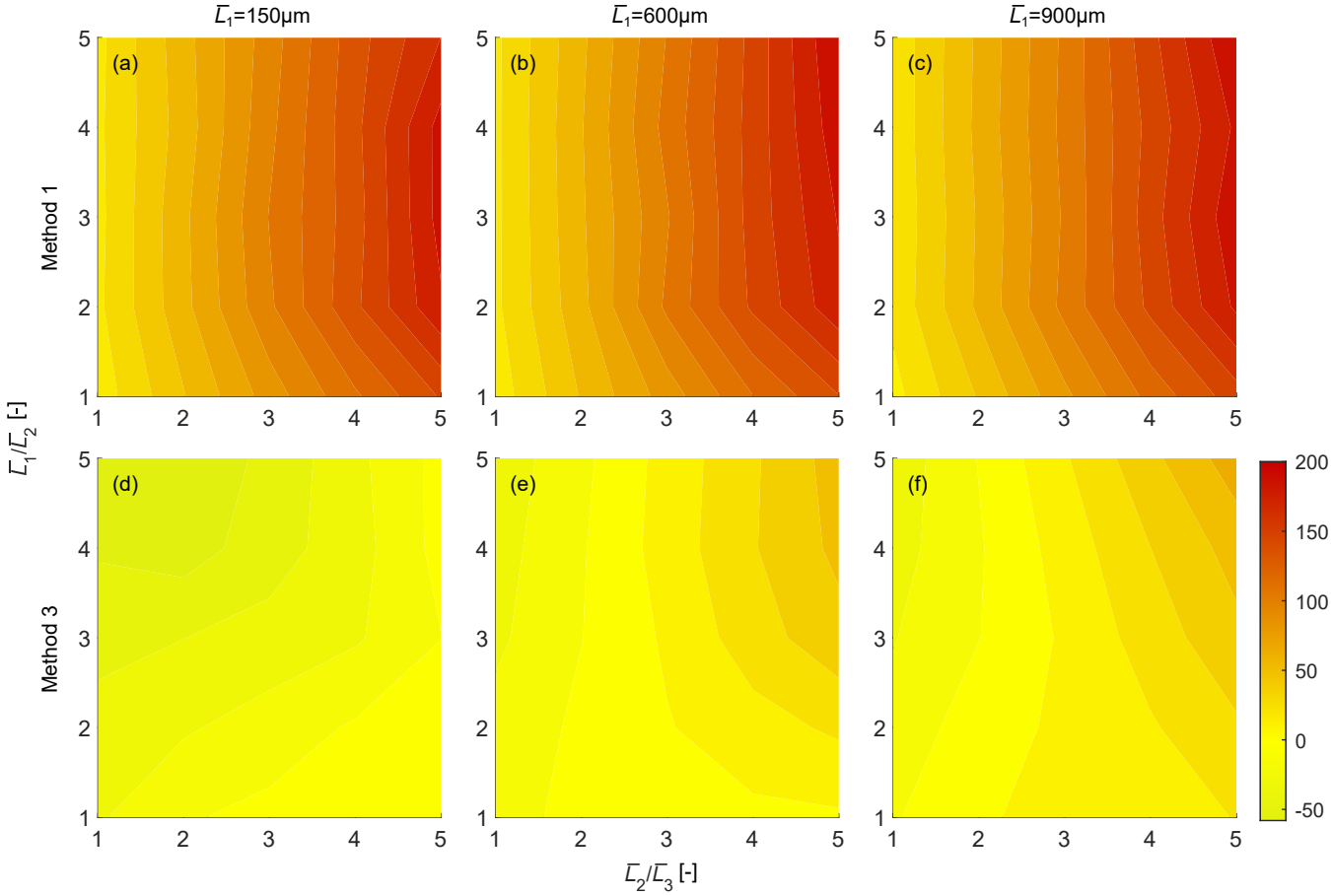

Figure S9: 2D contour plots of the average relative error $e_{\mathrm{rel}}(L_3)$ of the average thickness L_3 obtained using *method 1* (panels a-c) and *method 3* (panels d-f) as a function of the average aspect ratios of the true population $\bar{L}_1/\bar{L}_2$ and $\bar{L}_2/\bar{L}_3$ with different reference length $\bar{L}_{1,\mathrm{n}}$. This reference length in panels (a) and (d) is 150 μm, in panels (b) and (e) is 600 μm, and in panels (c) and (f) is 900 μm. Note that the relative error is computed using the number-weighted average over the entire true population and estimated population.

of 150 μm, 300 μm, 450 μm, 600 μm, 750 μm and 900 μm. Note that the uniform angle distribution (alignment case 3) is used in all these plots. Figure S9 shows the relative error on the third length $\bar{L}_3$ averaged over the entire population for three different reference lengths, namely 150 μm, 600 μm and 900 μm for both the techniques mentioned above. It is clear that for *method 1*, the absolute particle size does not have an influence on the error. In the case of *method 3*, there is a minor

dependence of the average error on the overall size, but this error stays below 50 % in all the cases.

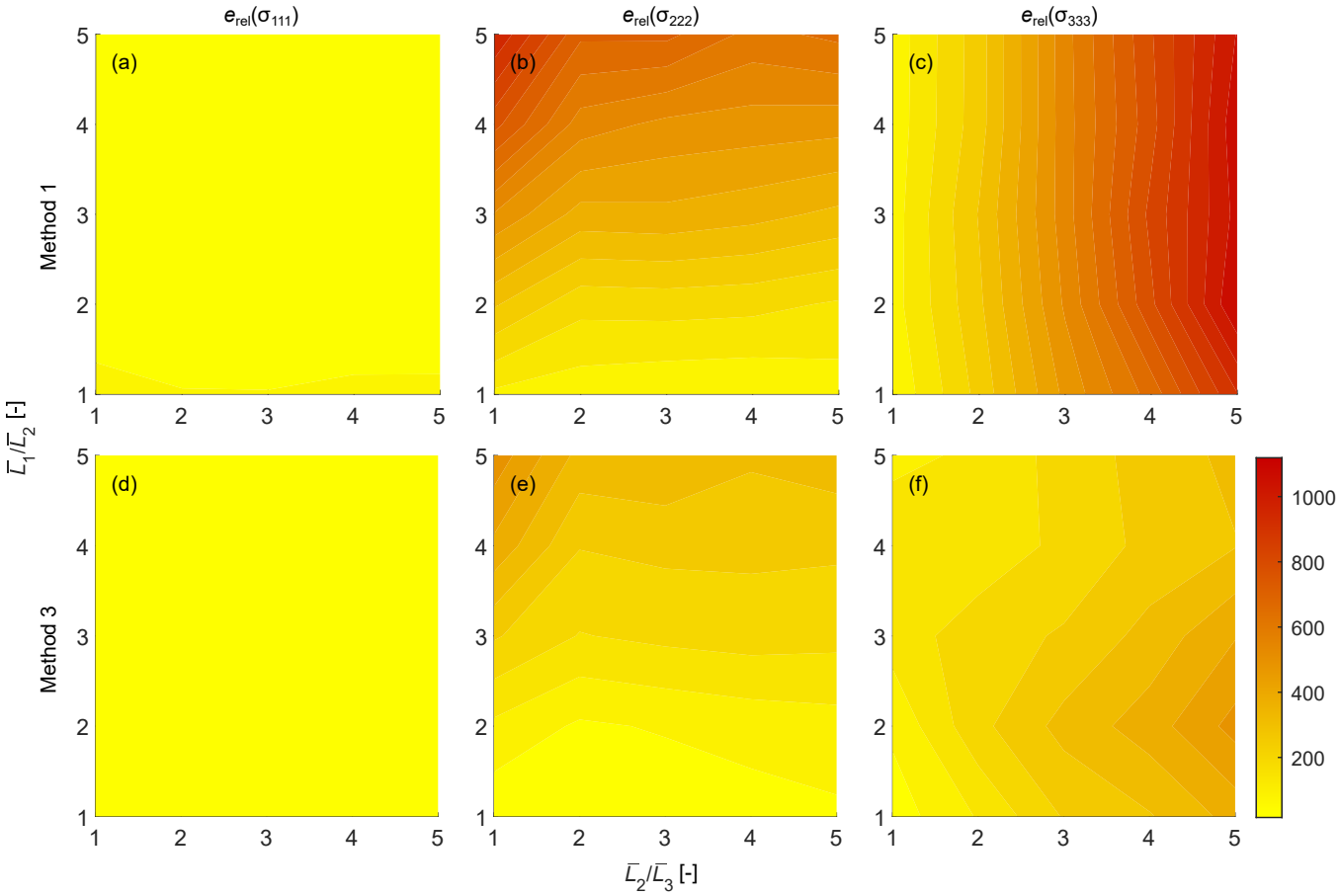

Figure S10: 2D contour plots of the relative error on distribution width along each length i $e_{rel}(\sigma_{iii})$ as a function of the average aspect ratios of the true population $\bar{L}_1/\bar{L}_2$ and $\bar{L}_2/\bar{L}_3$ with a reference length $\bar{L}_{1,n}$ of 150 µm. Panels (a) through (c) visualize this error for *method 1*, while panels (d) through (f) visualize this error for the dual projection imaging algorithms coupled with the machine learning model.

Figure S10 shows the influence of the average aspect ratios on the relative error of the distribution width σ_{iii} along the the three lengths. Panels (a) to (c) display the effect of this dependence on the estimates obtained by using *method 1*, and panels (d) to (f) for estimates obtained using *method 3*. Among the three lengths, the width along the third length σ_{333} has the highest error with both the methods. This could be due to the fact that the alignment dependence of particle characterization leads to a wide distribution of estimated thickness $\hat{L}_3$. However, the machine learning model reduces

the relative error on the distribution width by about half when compared to *method 1*. Unlike the errors on the average lengths, the errors on the distribution width are still significant.

S4.5 Model Retraining for Ideal Alignment Case

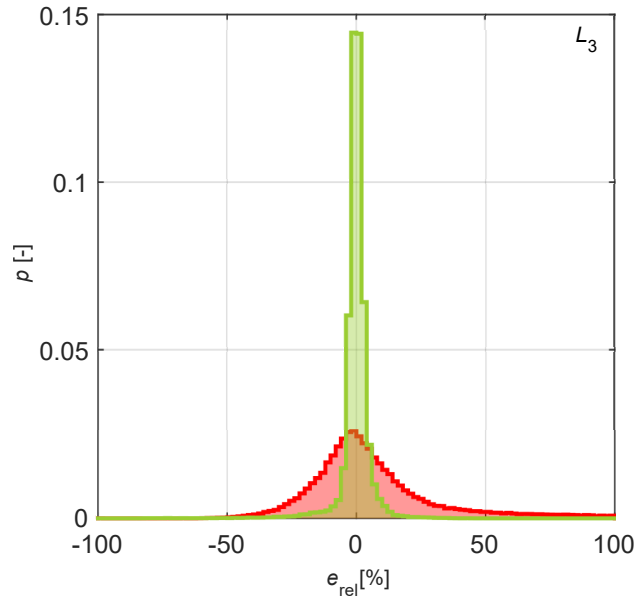

Figure S11: Distribution of the relative errors e_{rel} on the characteristic length L_3 for dual projection coupled with two different models. One model (green) is trained and tested on perfectly aligned particles, and the other (red) is trained and tested on randomly aligned particles. Note that both the models are trained and tested on the same particle populations, with identical hyperparameters. The bin size for the distribution is 2 %.

From Section 4.2 of the main text, it is clear that the machine learning model still exhibits a 33 % average error and an aspect ratio dependency, but to a lesser extent when compared to *method 1*. This can be attributed to multiple factors. First, a suboptimal model optimization and/or a lack of useful information in the feature set due to the features chosen for the model training. Second, the inability to differentiate between a diagonally aligned plate-like particle and an equant particle facing the camera (see Figure 2 of the main text), meaning a lack of information inherent in the

available image. In order to test if the error observed is an artifact of the particle alignment and the lack of information in the feature set, the model is retrained with identical hyperparameters on the same populations as in the training data set pictured in Figure S6. However, instead of a random particle alignment, all the particles are perfectly aligned with the camera (see case (1) in Section 3.1 of the main text). This model is then assessed on the same test set as the one used in previous subsections, but with perfectly aligned particles. If the reason for the error in the final model is due to alignment issues, the error using this newly built model on the perfect alignment case should tend toward zero. This is in turn what is observed in Figure S11. The distribution width of the relative errors on the third length (thickness), decreases significantly when training and testing on nicely aligned particles. The vast majority of the remaining model error is caused by the lack of information due to random alignment, and therefore cannot be reduced significantly by further feature engineering, an improved data sampling methodology or by a superior model optimization routine. However, it is acknowledged that the machine learning model is not free of errors even under ideal particle alignment (an average error of 3 %). In conclusion, the machine learning model described in the main text is the best possible model (under the constraints posed in this work).

S4.6 Model Error Distribution for Noncuboidal Particles

As a final comment, the performance of*method 3* on noncuboidal particles (e.g. hexagonal platelets, octagonal platelets, and parallelopipeds) is slightly worse than that of cuboidal platelets. The distribution of relative errors on the test set for different morphologies are shown in Figure S12. Model estimates for all lengths are slightly better for cuboids than for noncuboidal particles. This can be attributed to the fact that noncuboidal particles are significantly underrepresented in the data set, and therefore the model is incentivized to learn patterns better applicable to cuboidal particles.

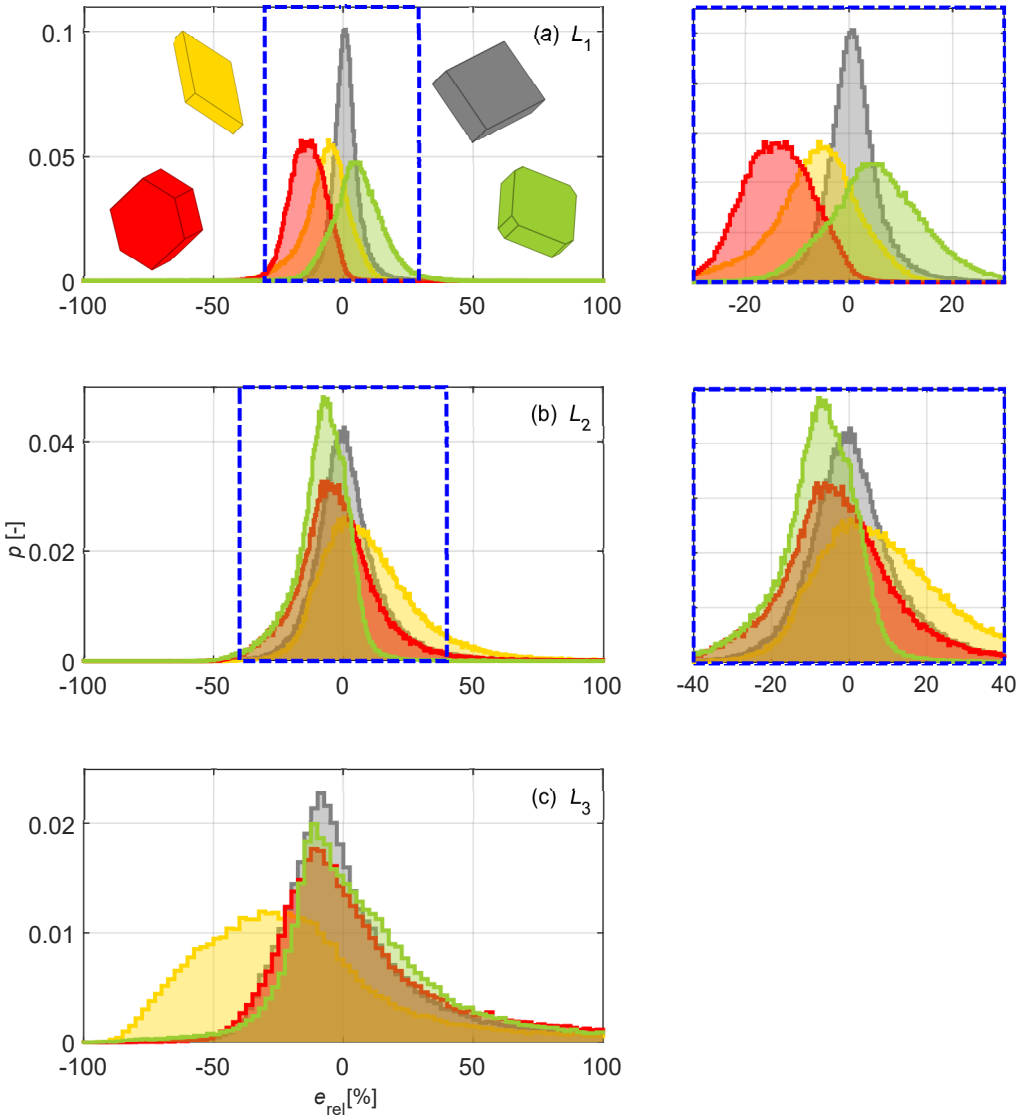

Figure S12: Distribution of the relative errors e_{rel} on the characteristic lengths for dual projection coupled with the model tested on four different test sets characterized by different morphology of the particles. These are cuboids (gray), diagonal platelets (yellow), hexagonal platelets (red), and octagonal platelets (green), as shown in panel (a). The bin sizes for the distributions are 1 %, 1 %, and 5 % for panel (a), (b), and (c), respectively. Zoomed in version of the plots for the region of interest (blue dotted box) are provided on the right hand side.

These patterns might not necessarily generalize well to other shapes. However, *method 3* still outperforms *method 1*, even on noncuboidal particles. In applications dealing with a specific type of crystal morphology, the model can be retrained on particles of that specific morphology to improve

the performance. Note that the target lengths in the case of noncuboids are given by the lengths of the oriented bounding box fitted to the original particle.

S5 Modeling a Crystallization Process

S5.1 Population Balance Equation Framework

The growth of an ensemble of platelets in suspension can be modeled using a morphological *Population Balance Equation* (PBE). As discussed in Section 2.1 of the main text, the platelets in this work are approximated using a generic particle shape model characterized using three lengths. In reality, crystals are multifaceted complex polyhedra, which are approximated as a cuboid in the image analysis pipeline for reasons reported elsewhere.[2] Here, however, the simulated crystal population is assumed to be exhibit a cuboidal shape for the sake of simplicity. Under this assumption, the PBE describing the evolution of an ensemble of crystals (seeds) subjected to growth only, i.e. in the absence of nucleation, agglomeration or breakage, can be formulated as

$$\frac{\partial f}{\partial t} + G_1 \frac{\partial f}{\partial L_1} + G_2 \frac{\partial f}{\partial L_2} + G_3 \frac{\partial f}{\partial L_3} = 0 \tag{S1}$$

where $f(t, L_1, L_2, L_3)$ [$\mu\text{m}^{-3}\,\text{kg}^{-1}$] is the number density function (called PSSD for the sake of brevity), defined on a per mass of solvent basis, and G_i [$\mu\text{m}\,\text{s}^{-1}$] is the size-independent growth rate of the ith characteristic particle length ($i = 1, 2, 3$). In this work, G_i (given in Equation S2) is assumed to be a function of the temperature T [°C] and of the relative supersaturation $S = c/c^*(T)$ [–], where c [$\text{g}\,\text{kg}^{-1}$] is the solute concentration defined on a per mass of solvent basis and $c^*(T)$ is the corresponding solubility at temperature T.

$$G_i = k_{1,i}(S-1)^{k_{2,i}} \exp\left(\frac{-k_{3,i}}{T + 273.15}\right) \tag{S2}$$

The PBE given in Equation S1 requires the following initial and boundary conditions

$$f(0, L_1, L_2, L_3) = f_0(L_1, L_2, L_3) \tag{S3}$$

$$f(t, \infty, L_2, L_3) = 0$$

$$f(t, L_1, \infty, L_3) = 0$$

$$f(t, L_1, L_2, \infty) = 0 \tag{S4}$$

where $f_0(L_1, L_2, L_3)$ is the PSSD of the seed population.

The PBE is additionally coupled with the material balance

$$\frac{\mathrm{d}c}{\mathrm{d}t} = -\rho_\mathrm{c} k_\mathrm{v} \frac{\mathrm{d}}{\mathrm{d}t} \int_0^\infty \int_0^\infty \int_0^\infty L_1 L_2 L_3 f\left(t, L_1, L_2, L_3\right) \mathrm{d}L_1 \, \mathrm{d}L_2 \, \mathrm{d}L_3 \tag{S5}$$

where ρ_c [g µm^{-3}] is the crystal density and k_v [–] is the volume shape factor. The initial condition for Equation S5 is $c(0) = c_0$, where c_0 is the initial solute concentration.

The integro-differential PBE model given by Equation (S1) to (S5) was solved numerically using a fully discrete high resolution finite volume method with the van Leer flux limiter.[3–5] For the simulations reported in this work, a regular grid with a grid spacing of 7 µm, 7 µm, and 7 µm along L_1, L_2, and L_3, respectively, was used; the corresponding number of grid intervals was 240, 240, and 40, respectively.

The average particle length $\bar{L}_1$, width $\bar{L}_2$, and thickness $\bar{L}_3$ of the population, obtained from the PSSD, are quantities of interest in this article. These average particle lengths can be weighed either on a number or on a volume basis.[2,6] The number-weighted average lengths $\bar{L}_{i,\mathrm{n}}$ $(i = 1, 2, 3)$ [µm]

will be used in this article and are defined as

$$\bar{L}_{1,\mathrm{n}}(t) = \frac{\mu_{100}(t)}{\mu_{000}(t)}$$
$$\bar{L}_{2,\mathrm{n}}(t) = \frac{\mu_{010}(t)}{\mu_{000}(t)}$$
$$\bar{L}_{3,\mathrm{n}}(t) = \frac{\mu_{001}(t)}{\mu_{000}(t)} \tag{S6}$$

where

$$\mu_{ijk}(t) = \int_0^\infty \int_0^\infty \int_0^\infty L_1^i L_2^j L_3^k f(t, L_1, L_2, L_3)\, \mathrm{d}L_1\, \mathrm{d}L_2\, \mathrm{d}L_3 \tag{S7}$$

is the ijk-cross moment [$\mu\mathrm{m}^{\mathrm{i+j+k}}\,\mathrm{kg}^{-1}$] of the PSSD f.

Likewise, the number-weighted width σ_{iii} ($i = 1, 2, 3$) [μm] of the PSSD at time t along each of the three lengths is defined as

$$\sigma_{111,\mathrm{n}}(t) = \sqrt{\mu_{200}(t)/\mu_{000}(t) - \left(\mu_{100}(t)/\mu_{000}(t)\right)^2}$$
$$\sigma_{222,\mathrm{n}}(t) = \sqrt{\mu_{020}(t)/\mu_{000}(t) - \left(\mu_{010}(t)/\mu_{000}(t)\right)^2}$$
$$\sigma_{333,\mathrm{n}}(t) = \sqrt{\mu_{002}(t)/\mu_{000}(t) - \left(\mu_{001}(t)/\mu_{000}(t)\right)^2} \tag{S8}$$

The populations in this article are visualized using a normalized number-weighted PSSD f_n [$\mu\mathrm{m}^{-3}$] which is defined as

$$f_\mathrm{n}(t, L_1, L_2, L_3) = \frac{f(t, L_1, L_2, L_3)}{\mu_{000}(t)} \tag{S9}$$

Since the particles and hence the population are characterized using three characteristic lengths, the PSSD translates into a three dimensional distribution. A two dimensional distribution can easily be represented using a three-dimensional surface density plot or a two-dimensional contour plot. However, for a three dimensional distribution, a four-dimensional surface density plot is required, which for obvious reasons cannot be used. Therefore, a three-dimensional contour plot is necessary

and to simplify the visualization, the three-dimensional contour plot is translated into three two-dimensional contour plots using the marginal distributions $f_{\mathrm{n},i}$ [$\mu\mathrm{m}^{-2}$] along the ith particle length defined as

$$f_{\mathrm{n},1}(t, L_2, L_3) = \int_0^\infty f_{\mathrm{n}}(t, L_1, L_2, L_3)\,\mathrm{d}L_1$$
$$f_{\mathrm{n},2}(t, L_1, L_3) = \int_0^\infty f_{\mathrm{n}}(t, L_1, L_2, L_3)\,\mathrm{d}L_2$$
$$f_{\mathrm{n},3}(t, L_1, L_2) = \int_0^\infty f_{\mathrm{n}}(t, L_1, L_2, L_3)\,\mathrm{d}L_3 \tag{S10}$$

Note that the distributions in Equation S10 are obtained by stacking the particles and summing them along a given dimension. It is worth noting that Equation (S6) to (S10) can also be applied to the estimated distributions and these quantities will be differentiated from the true distribution or the distribution from the PBE model using the hat symbol (e.g. $\hat{f}$, $\hat{\bar{L}}_{1,\mathrm{n}}$).

In this article, the population obtained from the PBE solver $f(t, L_1, L_2, L_3)$ is then sampled and processed using the methodology described in Section 2.1 of the main text, to yield an estimated population $\hat{f}(t, L_1, L_2, L_3)$. This serves as a proxy to visualize a real crystallization experiment, where the PBE solver simulates the physics of the growth process and the processing methodology (see Section 2.1 of the main text) serves as a simulation of the imaging sensor to observe the growth process. It is expected that the distributions obtained from the latter will be different from the former due to the errors associated with the characterization technique.

S5.2 Kinetic Growth Parameters

The kinetic constants $k_{\mathrm{g},i,1}$ in Equation S2 are varied for the three lengths so as to transform an equant particle toward a platelet shape. The values of the kinetic parameters along all the three lengths appearing in the growth rate equation are provided in Table S2.

The solubility c^* of the hypothetical compound, used to compute the supersaturation S, is given as

$$c^*(T) = 3.37\mathrm{e}^{0.0359T}\,[\mathrm{g\,kg^{-1}}] \tag{S11}$$

The crystal density ρ_C of the compound was set to $1590\,\mathrm{kg\,m^{-3}}$.

Table S2: Parameter values for the growth rates G_i in Equation S2 along length i.

	$i = 1$	$i = 2$	$i = 3$
$k_{\mathrm{g},i,1}$ [$\mu\mathrm{m\,s^{-1}}$]	240 000	200 000	40
$k_{\mathrm{g},i,2}$ [–]	3	3	3
$k_{\mathrm{g},i,3}$ [K]	2500	2500	2500

S5.3 Operating Conditions

The time-resolved evolution of the temperature and the evolution of the solute concentration in the simulation study described in Section 5 of the main text are visualized in Figure S13.

References

[1] Rajagopalan, A. K.; Schneeberger, J.; Salvatori, F.; Bötschi, S.; Ochsenbein, D. R.; Oswald, M. R.; Pollefeys, M.; Mazzotti, M. *Powder Technol.* **2017**, *321*, 479–493.

[2] Schorsch, S.; Vetter, T.; Mazzotti, M. *Chem. Eng. Sci.* **2012**, *77*, 130–142.

[3] LeVeque, R. J. *Finite Volume Methods for Hyperbolic Problems*; Cambridge Texts in Applied Mathematics; Cambridge University Press: Cambridge, UK, 2002; Vol. 31.

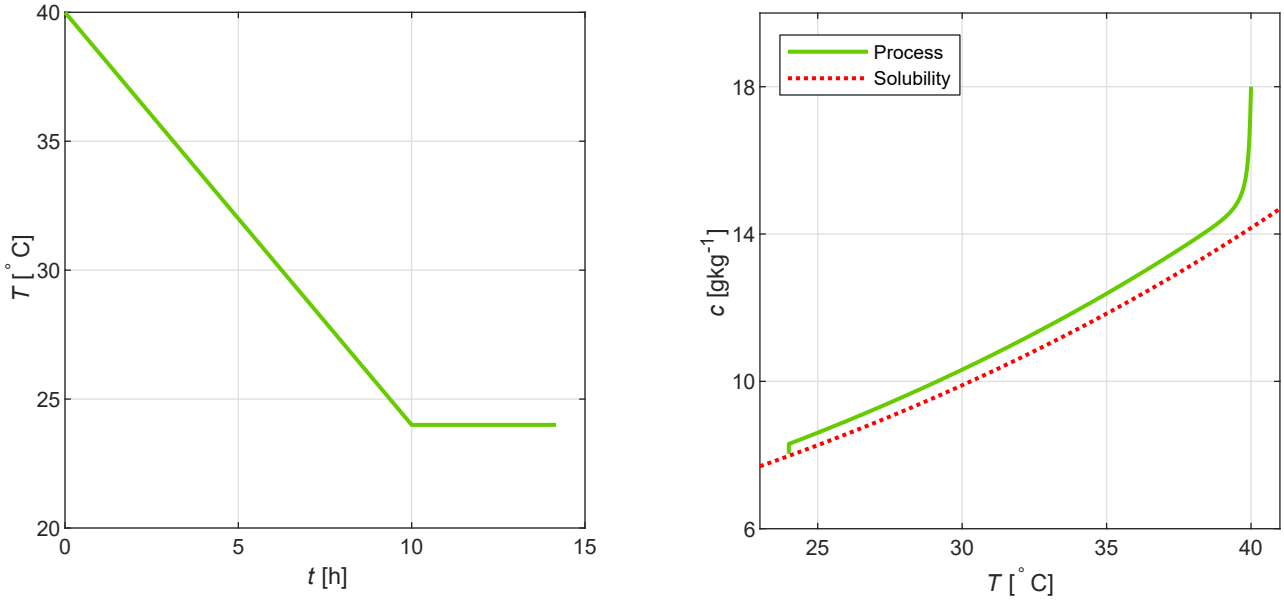

Figure S13: (a) Temperature profile of the simulated crystallization process and (b) the corresponding evolution of the solute concentration as a function of temperature (green) contrasted with the solubility curve of the plate-like compound obtained using Equation S11 (red).

[4] Ma, D. L.; Tafti, D. K.; Braatz, R. D. *Ind. Eng. Chem. Res.* **2002**, *41*, 6217–6223.

[5] Gunawan, R.; Fusman, I.; Braatz, R. D. *AIChE J.* **2004**, *50*, 2738–2749.

[6] Schorsch, S.; Ochsenbein, D. R.; Vetter, T.; Morari, M.; Mazzotti, M. *Chem. Eng. Sci.* **2014**, *105*, 155–168.